CONDENSED MATTER PHYSICS

Observation and control of spontaneous magnon emission from spin ensembles in 2D hexagonal boron nitride

Ling-Jie Zhou[1], Jayakrishnan M. P. Nair[2]†, Senlei Li[1], Thomas Poirier[3], Yiran Zhao[1], Zelong Xiong[1], Sumedh Rathi[1], Jingcheng Zhou[1], Zhigang Jiang[1], Hailong Wang[1], James H. Edgar[3], Benedetta Flebus[2]*, Chunhui Rita Du[1]*

Copyright © 2026 The Authors, some rights reserved; exclusive licensee American Association for the Advancement of Science. No claim to original U.S. Government Works. Distributed under a Creative Commons Attribution NonCommercial License 4.0 (CC BY-NC).

Hybrid systems consisting of color centers and magnetic materials provide an appealing solid-state platform for advancing the burgeoning quantum technological revolution. Exploring previously unknown coupling mechanisms between optically active spin defects and quantum degrees of freedom is directly relevant in this context. Here, we report observation and control of spontaneous magnon emission from boron-vacancy centers in two-dimensional hexagonal boron nitride (hBN) to a proximal ferrimagnet in the near-zero–temperature limit. The spontaneous magnon emission process is overshadowed by thermal magnon effect as temperature increases, reflecting the crossover from a spontaneous-emission–dominated magnon reservoir to a thermally occupied spin bath where absorption and stimulated processes restore balance. By increasing the spin defect density, we further present that spontaneous magnon emission into a common spin bath could help establish magnon-mediated correlations in dense hBN spin ensembles. Our results are quantitatively captured by theoretical modeling, bringing insights into understanding qubit-magnon coupling, correlated spin dynamics, and many-body physics of color centers in the quantum regime.

INTRODUCTION

Harnessing dipole interaction between color centers and quantum degrees of freedom opens a promising route for implementing cutting-edge technological innovations in quantum metrology, quantum optics, and quantum information science (*1*–*8*). Exploring advanced material and qubit platforms with improved solid-state scalability, versatile dipole coupling, and previously unknown coupling channels serves as an important step for fulfilling this goal. Optically active spin defects contained in layered van der Waals (vdW) crystals are naturally relevant in this context (*9*–*12*). Taking advantage of excellent two-dimensional (2D) vdW compatibility and on-chip integrability, this class of spin defects can be arranged in nanoscale proximity of target materials and devices in an accessible and controllable way, showing great promise for revolutionizing the performance on spatial resolution, field sensitivity, and measurement modality of current quantum sensing technologies (*9*–*11*, *13*–*22*). To date, experimental detection of magnons, spins, and electric charges in various hard and soft material systems has been demonstrated by hexagonal boron nitride (hBN)–based quantum microscopy (*12*, *13*, *15*, *17*, *18*, *23*–*26*).

Despite the progress made thus far, the ongoing research on hBN spin defects is mostly limited to the conventional ^{4}He cryogenic temperatures (*16*, *23*, *27*, *28*), which provides only a subset of information about their intriguing quantum mechanical properties. The underlying spin relaxation mechanism, spin-phonon interaction, spin-spin correlations of hBN color centers, and their dipole coupling with other quantum degrees of freedom in sub-Kelvin regime where thermally induced decoherence and energy dissipation are effectively suppressed await exploration. This knowledge is crucial for designing hybrid systems with desirable quantum spin properties for realizing transformative quantum revolution (*29*–*31*).

Here, we report dipole coupling observed between boron-vacancy V_B^- centers in 2D hBN and magnons, bosonic quasiparticles carrying spin angular momentum, at millikelvin temperatures. We show that the intrinsic V_B^- spin relaxation rate markedly decreases by orders of magnitude when the temperature is lowered from ~5 K to ~60 mK. Enjoying the extended spin relaxation times, we present experimental evidence of V_B^- spin transition–driven spontaneous magnon emission into a proximal spin bath in the near-zero–temperature limit, where thermally induced quantum decoherence and energy dissipation are virtually frozen (*2*, *4*, *5*). The spontaneous magnon emission process starts to be overshadowed by the thermal magnon effect as temperature increases, reflecting the crossover from a spontaneous emission-dominated, effectively cold magnon reservoir to a thermally occupied bath where absorption and stimulated processes restore balance to erase the quantum signatures. By increasing the spin defect density, we further show that spontaneous magnon emission into a common spin bath from hBN spin ensembles could establish correlations between them, resulting in enhanced magnon-induced V_B^- spin relaxation rate. Our results are quantitatively captured by theoretical models, bringing insights into developing next-generation hybrid quantum magnonic systems composed of solid-state spin defects and magnetic materials (*2*, *32*).

RESULTS

Spin relaxation of hBN defects in the near-zero–temperature limit

We first briefly review the pertinent properties of hBN spin defects used in the current study. Figure 1A shows the atomic structure of

[1]School of Physics, Georgia Institute of Technology, Atlanta, GA 30332, USA. [2]Department of Physics, Boston College, Chestnut Hill, MA 02467, USA. [3]Tim Taylor Department of Chemical Engineering, Kansas State University, Manhattan, KS 66506, USA. *Corresponding author. Email: benedetta.flebus@bc.edu (B.F.); cdu71@gatech.edu (C.R.D.)
†Present address: Department of Physics and Astronomy, University of Delaware, Newark, DE 19716, USA.

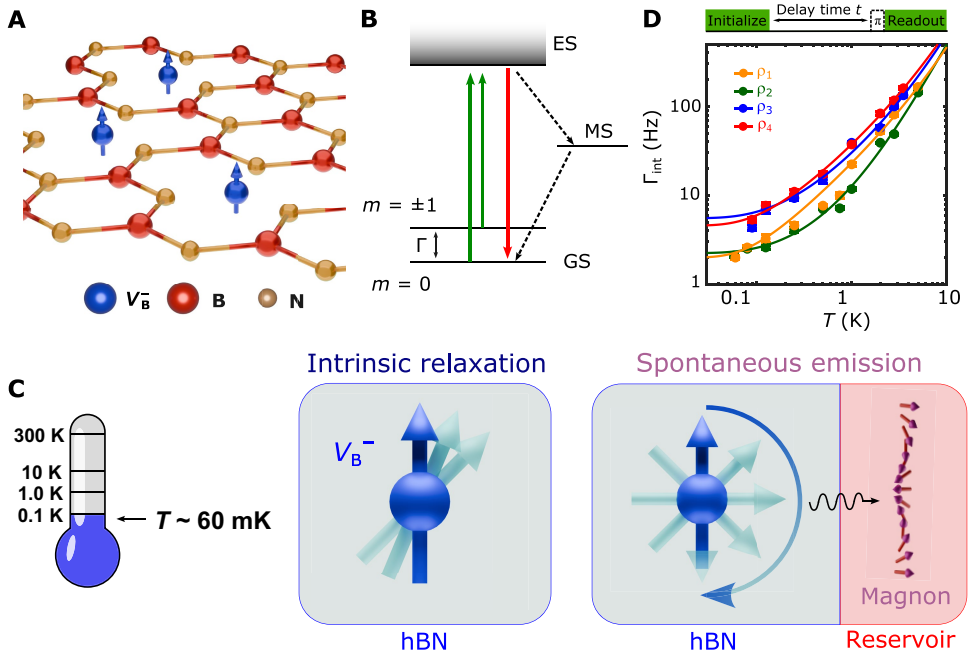

Fig. 1. Quantum spin relaxation of boron-vacancy centers in near-zero–temperature limit. (**A**) V_B^- spin defects (blue) formed in the hBN crystal structure with alternating boron (red) and nitrogen (brown) atoms. (**B**) Energy level diagram of a V_B^- spin defect and the optical excitation (green arrow), radiative recombination (red arrow), and nonradiative decay (black dashed arrows) between the ground state (GS), excited state (ES), and metastable state (MS). (**C**) Schematics of intrinsic V_B^- spin relaxation dynamics and spontaneous magnon emission to a proximal spin reservoir in the near-zero–temperature limit. (**D**) Temperature dependence of intrinsic V_B^- spin relaxation rate Γ_{int} measured down to ~60 mK for V_B^- spin ensembles with four different spin defect densities (ρ_1, ρ_2, ρ_3, and ρ_4). Experimental results (dots) are fitted to the theoretical model (curves). Optical and microwave sequence for spin relaxometry measurements is depicted on top.

boron-vacancy centers formed in the 2D hBN crystal lattice with alternating boron and nitrogen atoms (see section S1 for details) (*9*, *10*, *13*, *14*, *19*, *21*, *22*, *27*). Each V_B^- spin defect is surrounded by three nearest-neighboring nitrogen atoms. The negatively charged V_B^- center has an $S = 1$ electron spin with an intrinsic quantization axis along the out-of-plane direction (*9*). Figure 1B plots the energy level diagram of a V_B^- defect. A V_B^- center excited to the $m_s = \pm 1$ spin states is more likely to relax through a nonradiative pathway back to the $m_s = 0$ ground state and emits reduced photoluminescence (PL) (*20*, *27*, *33*). By measuring PL as a function of the delay time t and fitting the data with an appropriate theoretical model (*34*, *35*), occupation probabilities of a V_B^- center can be quantitatively obtained, allowing for extraction of the spin relaxation rate (*16*, *23*). Conventional quantum spin relaxometry is typically performed at temperatures high enough to ensure a substantial thermal magnon population in the spin bath, thereby enhancing magnetic noise fluctuations and the corresponding sensor-magnon relaxation signals (*1*, *18*, *23*, *35*–*38*). However, this regime is not optimal for hybrid quantum magnonic platforms building on spin defects coupled to magnetic materials. The operation of such systems generally favors ultralow temperatures, where the thermal energy scale remains below the spin-defect transition frequency, thereby minimizing decoherence and suppressing unwanted dissipation (*2*, *4*, *5*).

The current study takes advantage of a millikelvin quantum sensing platform (see section S2 for details) to investigate spin relaxation dynamics of V_B^- spin ensembles in the quantum regime, i.e., $T \to 0$, as illustrated in Fig. 1C. For the intrinsic case, V_B^- spin relaxation is dominated by phonon processes in hBN lattices (*13*, *16*), presumably showing a slow PL decay rate with an extended spin lifetime. Our spin relaxometry measurements corroborate this point. Figure 1D presents temperature dependence of intrinsic spin relaxation rate Γ_{int} measured on V_B^- spin ensembles with an estimated defect density $\rho_1 = 1.7 \times 10^{17}$ cm^{-3}, $\rho_2 = 3.1 \times 10^{17}$ cm^{-3}, $\rho_3 = 6.8 \times 10^{17}$ cm^{-3}, and $\rho_4 = 1.7 \times 10^{18}$ cm^{-3} contained in hBN nanoflakes. Γ_{int} shows a marked decrease when temperature is lowered from 5 K to 60 mK. The temperature-dependent Γ_{int} can be fitted to a physically motivated model, suggesting a combination of one-phonon and two-phonon scattering–driven V_B^- spin relaxation (see section S3 for details). V_B^- centers exhibit intrinsic spin relaxation rates comparable to those of shallowly implanted nitrogen-vacancy centers in the sub-Kelvin temperature regime (see section S3 for details). When V_B^- spin defects are coupled with a magnetic material in the zero temperature limit, there are essentially no thermal magnons populated at the V_B^- spin energy in the magnon bath. In this limit, thermal magnon absorption and stimulated processes are effectively frozen out, as the relevant modes of the spin bath are nearly unoccupied. Instead, in direct analogy with vacuum-induced spontaneous emission in quantum optics, an excited V_B^- center relaxes by emitting a magnon into the quantum vacuum of the magnetic reservoir (Fig. 1C) (*39*). This reveals a spin-defect–magnon coupling channel—driven purely by quantum fluctuations of the bath—which is expected to dominate in the low-temperature regime but has remained experimentally unexplored.

Observation of spontaneous magnon emission from V_B^- centers

We now present experimental observation of spontaneous magnon emission from V_B^- spin defects in the near-zero–temperature limit. Figure 2A shows the schematic of our measurement platform where

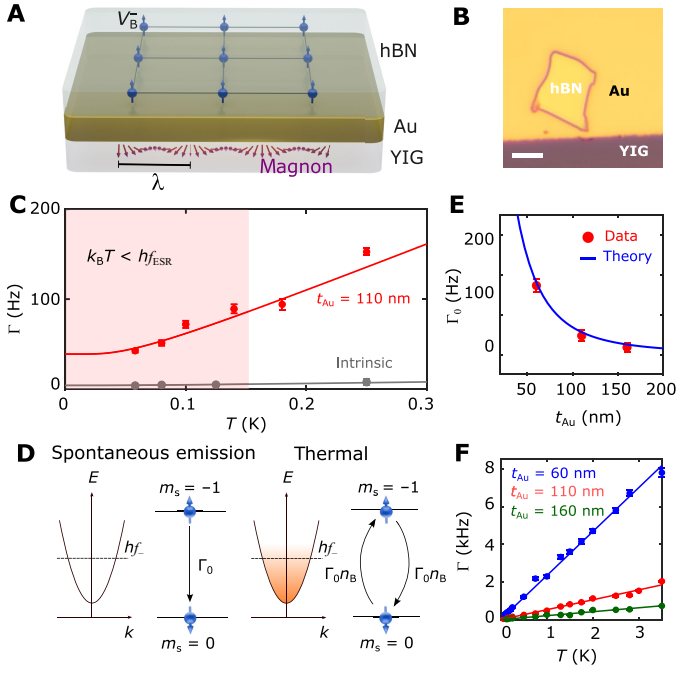

Fig. 2. Observation of spontaneous magnon emission from V_B^- centers. (**A**) Schematic view of our measurement platform where a hBN nanoflake containing V_B^- spin defects is transferred on top of an on-chip Au microwave stripline patterned on a 110-nm-thick YIG film. The spatial distribution of V_B^- spin defects is plotted in an illustrative way and not to scale. (**B**) Optical microscopy image of a prepared hBN/YIG device. Scale bar, 5 μm. (**C**) Temperature-dependent V_B^- spin relaxation rate Γ measured on a hBN/YIG sample in the sub-Kelvin regime. The estimated V_B^- spin defect density is $\rho_2 = 3.1 \times 10^{17}$ cm^{-3}, and the thickness of Au stripline is $t_{Au} = 110$ nm. The intrinsic V_B^- spin relaxation rate (gray color data points) is also presented for reference. (**D**) Schematic illustration of spontaneous magnon emission and thermal magnon effects on V_B^- spin relaxation in zero- and finite temperature regime. YIG magnon dispersion and band structure are plotted, and energy-dependent magnon density is highlighted by the fading colors. (**E**) Spontaneous magnon emission–induced V_B^- spin relaxation rate Γ_0 as a function of the Au stripline thickness t_{Au}. (**F**) Magnon-V_B^- dipole coupling–driven spin relaxation rate Γ measured up to ~3.5 K for three hBN/YIG samples with the same V_B^- spin defect density ($\rho_2 = 3.1 \times 10^{17}$ cm^{-3}) and different values of t_{Au}. Points in (C) and (F) denote experimental results, and solid lines (curves) represent theoretical calculations.

an exfoliated hBN nanoflake containing V_B^- ensembles is transferred onto an Au microwave stripline patterned on a 110-nm-thick $Y_3Fe_5O_{12}$ (YIG) film. Here, ferrimagnetic insulator YIG serves as a solid-state magnon bath proximal to V_B^- spin defects (*40*, *41*). An optical image in Fig. 2B provides an overview of a prepared hBN/YIG device for spin relaxometry measurements. Thickness of the hBN flake is ~75 nm (see section S1 for details), and microwave signals delivered into the on-chip Au stripline are used to provide local control of V_B^- spin states (*23*). The V_B^- spin defect density ρ is estimated to be 3.1×10^{17} cm^{-3}, and the thickness of the Au stripline t_{Au} is 110 nm (see Materials and Methods for details). Next, we report systematic spin relaxometry measurements on the hBN/YIG device in the sub-Kelvin regime. Figure 2C presents temperature-dependent V_B^- spin relaxation rate Γ measured from 58 to 300 mK (see section S4 for details). It is clear that the magnon-V_B^- coupling substantially enhances the V_B^- spin relaxation rate Γ compared with the intrinsic one.

We developed a detailed theoretical model to capture the transition from high-temperature thermal magnon effect to low-temperature spontaneous magnon-emission–induced V_B^- spin relaxation. Our discussion starts with a generic physical picture of dipole coupling between V_B^- centers and a YIG magnon bath. At thermal equilibrium, distribution of YIG magnons statistically follows the Bose-Einstein function: $n_B = \left(e^{hf/k_BT} - 1\right)^{-1}$, where n_B is the magnon occupation density, f is the magnon frequency, h is the Planck constant, and k_B is the Boltzmann constant. In the current study, our spin relaxometry experiments focus on YIG magnons at the lower spin transition ($m_s = 0 \longleftrightarrow -1$) of V_B^- electron spin resonance (ESR) frequency f_- (*2*, *35*). The observed V_B^- spin relaxation is mainly driven by two independent mechanisms: spontaneous magnon emission and thermal magnon effects. The spontaneous emission describes flipping of a V_B^- center from the $m_s = -1$ to $m_s = 0$ state that emits a magnon to the YIG spin bath at a rate of Γ_0 at zero temperature as illustrated in Fig. 2D (*39*). Using the fluctuation-dissipation theorem, Γ_0 can be expressed as (see section S5 for details) (*35*)

$$\Gamma_0 = \frac{1}{t_{hBN}} \iint_{t_{Au}}^{t_{Au}+t_{hBN}} D\left(f_-, \mathbf{k}\right) F(\mathbf{k}, t) d\mathbf{k} dt \qquad (1)$$

where D is the magnon spectral density, t is the distance between V_B^- centers and the top surface of the YIG film, t_{hBN} and t_{Au} are the thicknesses of hBN flake and Au stripline, respectively, and $F(\mathbf{k}, t)$ is the transfer function describing magnon-generated magnetic fields at V_B^- center sites. The thermal effect characterizes dipole coupling between V_B^- centers and a YIG magnon bath at a finite temperature, featuring direct magnon absorption and emission processes (at the V_B^- spin energy) that induce $m_s = 0 \longleftrightarrow -1$ spin relaxation (*35*). These magnon dynamics can be understood by invoking the Holstein-Primakoff transformation involving magnon creation or annihilation when the V_B^- frequency is above the YIG magnon bandgap energy. At a finite temperature, the thermally occupied magnon bath produces both absorption and stimulated-emission processes. For a single V_B^- center, the downward transition $m_s = -1 \rightarrow 0$ occurs at rate $\Gamma_0\left(1 + n_B\right)$, where the factor 1 represents spontaneous magnon emission and n_B represents stimulated emission. The upward transition $m_s = 0 \rightarrow -1$ occurs at rate $\Gamma_0 n_B$, corresponding to thermal magnon absorption. This asymmetric spin relaxation can be experimentally revealed by V_B^- PL measurements under different initialization and readout states (see section S4 for details). The measured V_B^- population relaxation rate is therefore the sum of the upward and downward rates

$$\Gamma = \Gamma_0\left(1 + 2n_B\right) = \Gamma_0\left(1 + \frac{2}{e^{hf_-/k_BT} - 1}\right) \qquad (2)$$

Our experimental results are in satisfactory agreement with the theoretical predictions. In the near-zero–temperature limit where the thermal energy is below the V_B^- ESR frequency (~150 mK), the YIG magnon occupation density $n_B < 1$ and the magnon bath is only weakly populated; thus, the spontaneous emission effect is more pronounced than or dominates over the thermal effect (*2*, *39*). We find that the measured V_B^- spin relaxation rate Γ decreases as the temperature reduces and ultimately saturates to the value of spontaneous magnon emission rate Γ_0 when $k_BT \ll hf_-$ (Fig. 2C). In our quantum sensing experiments, we prepared multiple samples with different thicknesses t_{Au} of the on-chip Au stripline to control spatial separation between the hBN nanoflake and YIG sample. For hBN/YIG samples with $t_{Au} = 60$, 110, and 160 nm, Γ qualitatively increases with the decreasing t_{Au}, showing that a reduced V_B^--to-magnon

distance will enhance the spontaneous magnon emission rate Γ_0, which is fundamentally governed by the V_B^--magnon dipole coupling (see section S4 for details). The excellent agreement between experimentally obtained Γ_0 and the theoretical model across varying t_{Au}, as summarized in Fig. 2E, corroborates observation of spontaneous magnon emission from V_B^- centers in the near-zero–temperature limit.

In the "high-temperature" regime where $k_B T \gg hf_-$, the measured spin relaxation is dominated by fluctuating magnetic fields generated from YIG thermal magnons. The Bose-Einstein distribution function is approximated to $n_B \approx \frac{k_B T}{hf_-}$, which is also referred to as the Rayleigh-Jeans distribution, and the overall YIG thermal magnon density is proportional to measurement temperature. Figure 2F plots Γ as a function of temperature up to ~3.5 K. One can see that the V_B^- spin relaxation rate exhibits a linear temperature dependence when above ~500 mK for the three hBN/YIG samples with different values of t_{Au}, highlighting the dominant thermal magnon effect when $k_B T \gg hf_-$.

Magnetic field control of spontaneous magnon emission of V_B^- centers

Because the V_B^--magnon dipole coupling serves as a driving force to the spontaneous magnon emission process, the measured V_B^- spin relaxation rates naturally inherit characteristics of the spin-wave dispersion of the magnetic material. Next, we tune the V_B^- spin transition frequency to show that the spontaneous magnon emission rate Γ_0 can be effectively controlled by the wave vector of the YIG magnon bath. Figure 3A plots a normalized spin wave transmission map of the 110-nm-thick YIG sample measured (see section S6 for details). The direction of the external magnetic field B_{ext} is 14° tilted away from the out-of-plane axis, which is the same as that in our V_B^- spin relaxometry measurements. At the ferromagnetic resonance (FMR) condition, a notable amount of microwave power is absorbed by the YIG magnetization, leading to a reduced microwave transmission efficiency characterized by S_{12} (*40*, *42*, *43*). The FMR frequency f_{FMR} defining the minimum YIG magnon energy increases with B_{ext}, and the energy difference between f_- and f_{FMR} continuously decreases with increasing B_{ext} in the magnetic field range surveyed. Thus, it is expected that a YIG magnon spontaneously emitted by the $m_s = -1 \rightarrow 0$ spin transition of a V_B^- center tends to have a larger wave vector in the low magnetic field regime and vice versa as shown by the YIG magnon wave vector k map in Fig. 3B (see section S6 for details). Figure 3C presents variations of Γ_0 as a function of the external magnetic field B_{ext}. The measured Γ_0 shows a monotonical decrease with B_{ext} for the three hBN/YIG samples surveyed and nicely follows the theoretical prediction (Eq. 1), demonstrating field control of spontaneous magnon emission rate of V_B^- centers. A slower spin relaxation rate observed in the higher magnetic field regime is attributed to the k-dependent transfer function $F(\mathbf{k}, t)$ that enters in the calculation of V_B^- spin relaxation rate (*35*). In the limit of $k < 1/t$, a high–wave vector YIG magnon is energetically more favorable to be emitted from a V_B^- center; thus, a higher magnon energy (f_-) at a lower magnetic field will give rise to an enhanced magnon emission rate (see section S5 for details). By setting the V_B^- ESR frequency to an arbitrary value in Eq. 1, we can further obtain a spontaneous magnon emission rate map as presented in Fig. 3D.

Magnon-mediated correlations in V_B^- spin ensembles

The spontaneous magnon emission observed at millikelvin temperatures opens a promising route for engineering magnon-mediated correlations in V_B^- spin ensembles. When V_B^- defects are coupled through a magnon bath, spin relaxation of the ensemble contains two major contributions: (i) the usual independent single-defect decay and (ii) interference terms that correlate magnon emission (or absorption) events from different spin defects. In the dilute regime, the relative phase accumulated between defects i and j, set by $e^{i\mathbf{k}\cdot(\mathbf{r}_i - \mathbf{r}_j)}$, varies rapidly from pair to pair, thereby suppressing interdefect coherence;

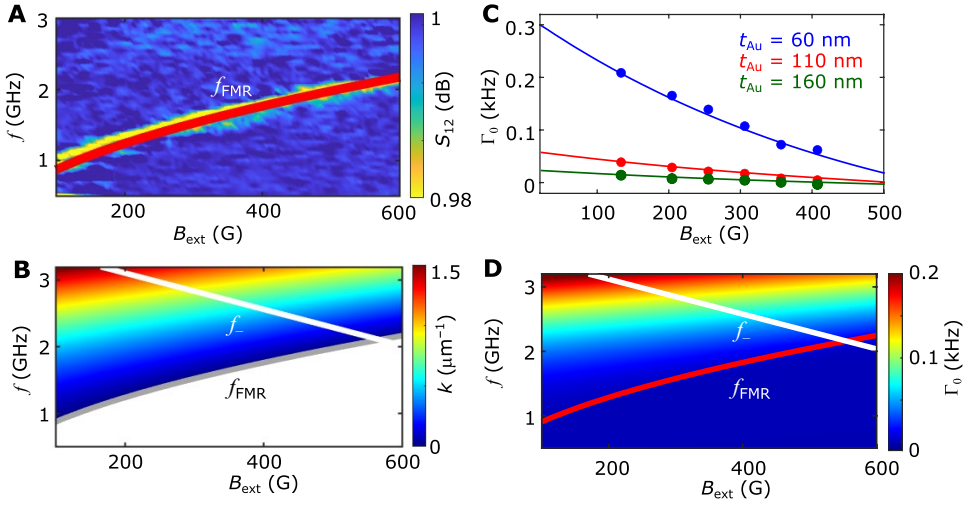

Fig. 3. Magnetic field control of spontaneous magnon emission rate of V_B^- centers. (**A**) FMR spin wave transmission map of a 110-nm-thick YIG film measured at 500 mK. The red curve highlights the YIG FMR frequency. (**B**) Theoretically calculated YIG magnon wave vector map with white and gray curves representing the V_B^- ESR frequency f_- ($m_s = 0 \leftrightarrow -1$) and the YIG FMR frequency f_{FMR}. (**C**) Spontaneous magnon emission rate Γ_0 measured as a function of the external magnetic field B_{ext}. The blue, red, and green data points correspond to three hBN/YIG samples with 60-, 110-, and 160-nm-thick on-chip Au striplines. The V_B^- spin defect density is estimated to be $\rho_2 = 3.1 \times 10^{17}$ cm^{-3} for the three hBN samples surveyed. Points are experimental results, and solid lines present theoretical calculations. Γ_0 values are extracted from temperature-dependent V_B^- spin relaxometry measurement down to sub-100 mK. (**D**) Theoretically calculated magnon emission rate Γ_0 map with white and red lines denoting the V_B^- ESR energy f_- ($m_s = 0 \leftrightarrow -1$) and the YIG FMR frequency f_{FMR}, respectively.

consequently, the ensemble relaxes essentially as a collection of independent defects (*2*). Here, $\mathbf{r}_i - \mathbf{r}_j$ is the separation vector between V_B^- defects. By contrast, in dense V_B^- ensembles with reduced inter-defect spacing, the magnon-mediated interference contributions can add constructively (*2*), potentially resulting in collective spin dynamics where spin relaxation ceases to be treated as independent depolarization of V_B^- centers and instead evolves to a correlated state with an enhanced relaxation rate as illustrated in Fig. 4A.

Figure 4B summarizes the estimated V_B^- spin density ρ of four hBN flakes with different neutron irradiation doses (see section S1 for details). Figure 4C presents four representative V_B^- spin relaxation spectra recorded at 90 mK. The V_B^- spin ensembles follow nearly identical relaxation behavior for $\rho_1 = 1.7 \times 10^{17}$ cm^{-3} and $\rho_2 = 3.1 \times 10^{17}$ cm^{-3}. As the spin defect density increases to $\rho_3 = 6.8 \times 10^{17}$ cm^{-3} and $\rho_4 = 1.7 \times 10^{18}$ cm^{-3}, the PL spectra of V_B^- spin ensembles exhibit a faster decay, reflecting an enhanced relaxation rate. By fitting our results to an exponential decay function, magnon-driven V_B^- spin relaxation rate Γ can be obtained as summarized in Fig. 4D (see section S4 for details). We developed a correlated spin defect model to account for spin defect–density–dependent V_B^- relaxation. Correlated V_B^- spin relaxation rate can be approximately described by the following expression (see sections S7 and S8 for details)

$$\Gamma = \sqrt{(A+B)^2 - 4AC} \tag{3}$$

where $A = \eta\Gamma_0\lambda^2 t_{hBN}\rho$ represents the correlated magnon emission contribution, $B = \Gamma_0(1+2n_B)$ is the uncorrelated spin relaxation rate considering both spontaneous emission and thermally driven transitions, and $C = \Gamma_0 n_B$ characterizes the contribution from thermal magnon absorption. λ is the wavelength of the magnons resonant with the spin-defect transition frequency f_-, and η is a phenomenological parameter, which rescales spin defect number and defines an effective V_B^- density in our model. When $\eta \to 0$, our model reduces to the independent spin dynamics and $\Gamma \to \Gamma_0(1+2n_B)$. Nonidealities such as local dephasing, inhomogeneous broadening, nonuniform coupling strengths, and disorder will suppress the correlation and further reduce from its ideal value (see section S7 for details). Substituting relevant material parameters into the above equation, theoretical calculations of Γ are presented in Fig. 4D.

Overall, our experimental results are in agreement with the model. For $\rho_1 = 1.7 \times 10^{17}$ cm^{-3} and $\rho_2 = 3.1 \times 10^{17}$ cm^{-3}, the measured Γ basically follows the theoretical prediction of $\Gamma_0(1+2n_B)$, indicating a largely uncorrelated V_B^- spin relaxation behavior in the dilute regime. In the high defect density regime, distinct V_B^- centers couple to resonant modes of the YIG magnon bath, enabling the bath to mediate nonlocal decay channels between different spin defects. Under these conditions, reservoir-induced cross couplings give rise to correlated spin relaxation dynamics, manifested as density-dependent deviations from the independent-defect decay (*2*). For $\rho_3 = 6.8 \times 10^{17}$ cm^{-3}, measured V_B^- spin relaxation rates are enhanced from the uncorrelated case due to the pronounced correlated magnon emission effect. Intuitively, a higher ρ reduces the typical defect-defect separation, so a single magnon mode can couple a larger number of defects within its spatial reach. When spin defect density increases to $\rho_4 = 1.7 \times 10^{18}$ cm^{-3}, the magnon-mediated correlation effect in V_B^- ensembles becomes more pronounced, as evidenced by the further increase in Γ. When normalized by the uncorrelated relaxation value, $\frac{\Gamma}{\Gamma_0(1+2n_B)}$ features substantial enhancement in the sub-Kelvin regime as shown in Fig. 4E. As expected, this enhancement is suppressed with increasing temperature. When $T > 1$ K, signatures of magnon-mediated correlation fully disappear, which is attributed to the dominant thermal magnon effect that overshadows correlated magnon emission of V_B^- centers (*2*), resulting in the absence of density-dependent effects and convergence of decay rates across different samples.

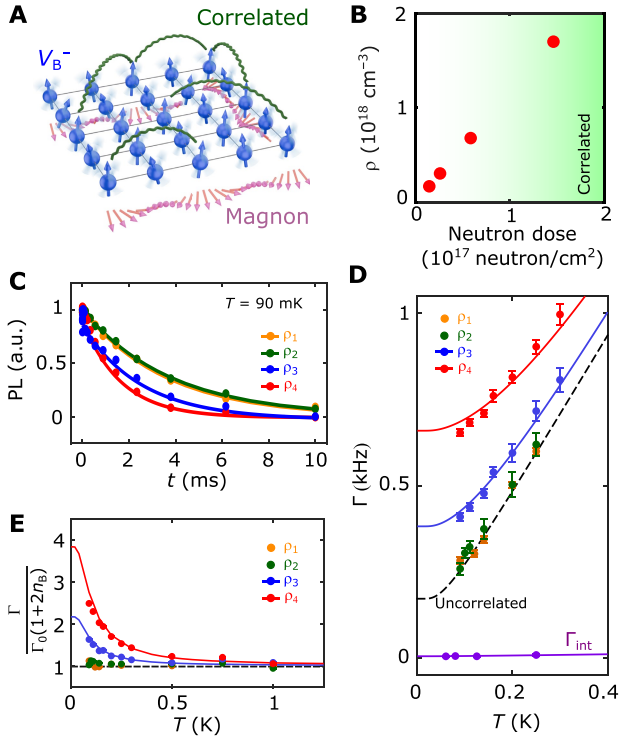

Fig. 4. Magnon-mediated correlated V_B^- spin relaxation. (**A**) Schematics of correlated relaxation of V_B^- spin ensembles when interfaced with a shared magnon bath. (**B**) V_B^- spin defect density ρ estimated as a function of the neutron irradiation dose. The fading green color indicates gradual transition from uncorrelated to correlated spin relaxation regime with increasing ρ. (**C**) Spin relaxation spectra of V_B^- ensembles with four different spin defect densities (ρ_1, ρ_2, ρ_3, and ρ_4) measured at 90 mK. Experimental results (dots) are fitted to exponential decay (lines). The thickness of the Au stripline is 60 nm for the four hBN/YIG samples surveyed. a.u., arbitrary units. (**D**) Spin relaxation rate Γ of V_B^- ensembles measured as a function of temperature in the sub-Kelvin regime. Results on four hBN samples with different V_B^- spin defect densities are presented. Black dashed lines represent theoretically calculated uncorrelated V_B^- spin relaxation rate $\Gamma_0(1+2n_B)$, and intrinsic spin relaxation rate Γ_{int} is also presented for reference. Experimental data sets of ρ_3 and ρ_4 are fitted to theoretical calculations (blue and red solid lines). (**E**) Magnon-driven V_B^- spin relaxation rate Γ normalized by the uncorrelated V_B^- spin relaxation rate in temperature range up to 1.25 K. Red and blue lines denote theoretical calculations. Black dashed lines represent the value of 1 for visual clarity.

DISCUSSION

In summary, we demonstrated millikelvin quantum sensing using boron-vacancy spin defects in 2D hBN nanoflakes. When lowering from ^{4}He cryogenic temperatures to the millikelvin regime, we observe orders of magnitude decrease in the intrinsic V_B^- spin relaxation rate due to suppression of phonon scattering–induced spin depolarization. Taking advantage of the extended V_B^- spin relaxation times, we introduce a shared YIG magnon bath to investigate dipole

coupling between V_B^- centers and a ferromagnetic spin bath, presenting clear evidence of spontaneous magnon emission from V_B^- centers in near-zero–temperature limit. By varying the spin defect density, we further explore experimental signatures of magnon-mediated correlated quantum spin relaxation dynamics of V_B^- ensembles. These results, reproduced well by our theoretical modeling, bring further insights into understanding collective spin dynamics, magnon-qubit coupling, and many-body physics of spin defects in the quantum regime (*2*). Our work also highlights the potential of magnons as mediating quanta capable of establishing long-range, tunable interaction between individual color centers and driving cooperative quantum effects such as super- and subradiant dynamics in strongly correlated spin defect ensembles (*1*, *4*, *5*, *31*, *44*–*47*). The hybrid systems consisting of magnons and hBN spin defects with tailored quantum mechanical properties also open avenues for developing cutting-edge technological innovations from sensing, metrology, and potentially to computing at the forefront of quantum revolution (*11*, *32*, *48*–*50*).

MATERIALS AND METHODS

Materials and device fabrications

The ^{10}B-enriched monoisotopic hBN crystals are synthesized using a metal (Ni-Cr) flux method (*51*). The starting materials include 48 wt % Ni (Alfa Aesar, 99.70%), 48 wt % Cr (Alfa Aesar, 99.99%), and 4 wt % ^{10}B (Ceradyne 3 M, 96.85%) powders. The source of elemental nitrogen is flowing natural N_2 gas (99.6% 14 N) or isotopically purified $^{15}N_2$ gas (99.7% 15 N), and H_2 gas is used to minimize impurities originating from oxygen and carbon (*52*). We use the thermal neutron irradiation method to create V_B^- spin defects in hBN crystals. The V_B^- spin defect density is controlled by the neutron irradiation time, which is set to be 1, 2, 4, and 10 hours, corresponding to a dose of $\sim 1.46 \times 10^{16}$, $\sim 2.63 \times 10^{16}$, $\sim 5.84 \times 10^{16}$, and $\sim 1.46 \times 10^{17}$ neutrons·cm^{-2}. The corresponding V_B^- spin defect density is estimated to be $\rho_1 = 1.7 \times 10^{17}$ cm^{-3}, $\rho_2 = 3.1 \times 10^{17}$ cm^{-3}, $\rho_3 = 6.8 \times 10^{17}$ cm^{-3}, and $\rho_4 = 1.7 \times 10^{18}$ cm^{-3} in the four types of hBN crystals studied.

hBN nanoflakes containing V_B^- centers are exfoliated onto Si/SiO_2 (285 nm) substrates. Selected hBN flakes are picked up by a stamp consisting of a thin layer of polycarbonate on polydimethylsiloxane (*53*) and then released onto an Au stripline patterned on Al_2O_3 or YIG(110 nm)/$Gd_3Ga_5O_{12}$ substrates. Residual polycarbonate on the device is dissolved in chloroform, and thickness of exfoliated hBN flakes is characterized by atomic force microscopy. Device preparation processes involving handling hBN nanoflakes are performed inside a glovebox filled with argon gas to minimize environmental effects. We prepared a series of hBN samples with different spin defect densities and Au stripline thicknesses for V_B^- spin relaxometry measurements. hBN samples on YIG(110 nm)/$Gd_3Ga_5O_{12}$ substrates are used for investigating magnon-driven spin relaxation of V_B^- spin ensembles. Samples prepared on Al_2O_3 substrates are used for studying intrinsic V_B^- spin relaxation properties. On-chip Au striplines with different thicknesses are patterned to investigate spatial separation dependence of the spontaneous magnon emission rate. YIG films grown on $Gd_3Ga_5O_{12}$ substrates are commercially available from the company Matesy GmbH.

Quantum spin relaxometry measurements

Pulsed V_B^- spin relaxometry measurements are performed using a custom-designed confocal microscopy built on a closed-loop dilution refrigerator. External magnetic fields are generated by a three-axis superconducting magnet, and the field direction is set to be 14° tilted away from the out-of-plane axis in our spin relaxometry measurements. Green laser pulses for V_B^- spin initialization and readout are generated by an electrically driven 515-nm laser. Laser power entering the optical objective is ~0.3 mW. Trigger pulses to the optical modulator and photon counter are generated by a programmable pulse generator, and microwave signals are modulated by a switch (Mini-Circuits ZASWA-2-50DR+). We use pulsed optical and microwave sequences for V_B^- spin relaxometry measurements. A green laser pulse is applied to prepare V_B^- spin defects to the $m_s = 0$ state. Then, V_B^- spins gradually relax into a mixture of $m_s = 0$ and $m_s = \pm 1$ states due to intrinsic and/or extrinsic depolarization effects. By measuring the delay time–dependent PL intensity integrated during the green-laser readout pulse and fitting the data to appropriate theoretical models, V_B^- spin relaxation rates can be quantitatively obtained.

Theoretical modeling of magnon-mediated correlated V_B^- spin relaxation

We model the V_B^- spin ensemble as an effective "two-level" spin system collectively coupled to a single intermediary reservoir mode. The dissipative dynamics of the ensemble can be described by a Lindblad master equation governing the correlated emission and absorption processes

$$\dot{\rho}_s = \Gamma_0 (n_B + 1) \mathcal{D}[J_-]\rho_s + \Gamma_0 n_B \mathcal{D}[J_+]\rho_s \quad (4)$$

which captures the interplay between decay and thermal excitation of the collective spin ensemble. Here, ρ_s is the density matrix, the single-spin rate Γ_0 is obtained from exponential fitting of the PL data for the case of a collection of uncorrelated spins, n_B denotes the thermal occupation of the spin reservoir, $J_\pm = \sum_i \sigma_i^\pm$ are the collective operators, and $\mathcal{D}[L]\rho_s = L\rho_s L^\dagger - \frac{1}{2}\{L^\dagger L, \rho_s\}$ represents the standard Lindblad dissipator. We note that Eq. 4 implicitly assumes that all spin defects participate collectively, forming a single large spin **J** that decays coherently into a magnon mode. In our experiments, however, bath-mediated correlations extend only over a finite spatial range. A fully microscopic treatment of $\sim 10^6$ inhomogeneously coupled spin defects interacting with a continuum of magnon modes is computationally intractable. We therefore use an effective description in which finite-range bath coherence and other sample-specific nonidealities are absorbed into a dimensionless parameter $\alpha \in [0, 1]$ fixed for each sample.

Here, $\alpha \to 1$ corresponds to the Dicke limit, while $\alpha \to 0$ describes independent spin dynamics. A simple scaling estimate yields $\alpha = \eta\lambda^2 t_{hBN}/V$, where V denotes the volume of the hBN sample and η is a phenomenological parameter obtained from fitting the experimental data. This reflects the fact that only spins within a wavelength-sized correlation patch remain phase locked, implying that longer magnon wavelengths enhance the collective contribution in Eq. 4. The dimensionless parameter α extracted from experimental data is 2.9×10^{-7}. This minimal parameterization satisfactorily reproduces the key experimental features and trends observed under variations of temperature and related parameters.

Supplementary Materials

This PDF file includes:

Supplementary Text
Sections S1 to S8
Table S1
Figs. S1 to S9
References

REFERENCES

1. D. D. Awschalom, C. R. Du, R. He, F. J. Heremans, A. Hoffmann, J. Hou, H. Kurebayashi, Y. Li, L. Liu, V. Novosad, J. Sklenar, S. E. Sullivan, D. Sun, H. Tang, V. Tyberkevych, C. Trevillian, A. W. Tsen, L. R. Weiss, W. Zhang, X. Zhang, L. Zhao, C. W. Zollitsch, Quantum engineering with hybrid magnonic systems and materials. *IEEE Trans. Quantum Eng.* **2**, 10.1109/TQE.2021.3057799 (2021).
2. X. Li, J. Marino, D. E. Chang, B. Flebus, Solid-state platform for cooperative quantum dynamics driven by correlated emission. *Phys. Rev. B* **111**, 064424 (2025).
3. C. L. Degen, F. Reinhard, P. Cappellaro, Quantum sensing. *Rev. Mod. Phys.* **89**, 035002 (2017).
4. L. Trifunovic, F. L. Pedrocchi, D. Loss, Long-distance entanglement of spin qubits via ferromagnet. *Phys. Rev. X* **3**, 041023 (2013).
5. M. Fukami, D. R. Candido, D. D. Awschalom, M. E. Flatté, Opportunities for long-range magnon-mediated entanglement of spin qubits via on- and off-resonant coupling. *PRX Quantum* **2**, 040314 (2021).
6. P. Put, N. T. Leitao, H. Gao, C. Spaegele, O. Makarova, L. B. Hughes Wyatt, A. C. Maccabe, M. Mammen, B. Machielse, H. Zhou, S. Pustelny, A. C. Bleszynski Jayich, F. Capasso, L. S. Martin, H. Park, M. D. Lukin, Collective many-body dynamics in a solid-state quantum sensor controlled through nanoscale magnetic gradients. arXiv:2506.11920 [quant-ph] (2025).
7. Z. Wu, P. Wang, T. Wang, Y. Li, R. Liu, Y. Chen, X. Peng, R.-B. Liu, Selective detection of dynamics-complete set of correlations via quantum channels. *Phys. Rev. Lett.* **132**, 200802 (2024).
8. A. Salhov, Q. Cao, J. Cai, A. Retzker, F. Jelezko, G. Genov, Protecting quantum information via destructive interference of correlated noise. *Phys. Rev. Lett.* **132**, 223601 (2024).
9. A. Gottscholl, M. Kianinia, V. Soltamov, S. Orlinskii, G. Mamin, C. Bradac, C. Kasper, K. Krambrock, A. Sperlich, M. Toth, I. Aharonovich, V. Dyakonov, Initialization and read-out of intrinsic spin defects in a van der Waals crystal at room temperature. *Nat. Mater.* **19**, 540–545 (2020).
10. X. Gao, S. Vaidya, K. Li, P. Ju, B. Jiang, Z. Xu, A. E. L. Allcca, K. Shen, T. Taniguchi, K. Watanabe, S. A. Bhave, Y. P. Chen, Y. Ping, T. Li, Nuclear spin polarization and control in hexagonal boron nitride. *Nat. Mater.* **21**, 1024–1028 (2022).
11. H. L. Stern, C. M. Gilardoni, Q. Gu, S. Eizagirre Barker, O. F. J. Powell, X. Deng, S. A. Fraser, L. Follet, C. Li, A. J. Ramsay, H. H. Tan, I. Aharonovich, M. Atatüre, A quantum coherent spin in hexagonal boron nitride at ambient conditions. *Nat. Mater.* **23**, 1379–1385 (2024).
12. H. Sun, P. Yu, X. Zhou, X. Ye, M. Wang, Z. Liu, Y. Guo, W. Liu, Y. Huang, P. Wang, F. Shi, K. Xia, Y. Wang, Room-temperature hybrid 2D-3D quantum spin system for enhanced magnetic sensing and many-body dynamics. *npj Quantum Inform* **12**, 10 (2026).
13. R. Gong, X. Du, E. Janzen, V. Liu, Z. Liu, G. He, B. Ye, T. Li, N. Y. Yao, J. H. Edgar, E. A. Henriksen, C. Zu, Isotope engineering for spin defects in van der Waals materials. *Nat. Commun.* **15**, 104 (2024).
14. A. Haykal, R. Tanos, N. Minotto, A. Durand, F. Fabre, J. Li, J. H. Edgar, V. Ivády, A. Gali, T. Michel, A. Dréau, B. Gil, G. Cassabois, V. Jacques, Decoherence of V_B^- spin defects in monoisotopic hexagonal boron nitride. *Nat. Commun.* **13**, 4347 (2022).
15. A. J. Healey, S. C. Scholten, T. Yang, J. A. Scott, G. J. Abrahams, I. O. Robertson, X. F. Hou, Y. F. Guo, S. Rahman, Y. Lu, M. Kianinia, I. Aharonovich, J.-P. Tetienne, Quantum microscopy with van der Waals heterostructures. *Nat. Phys.* **19**, 87–91 (2023).
16. A. Gottscholl, M. Diez, V. Soltamov, C. Kasper, A. Sperlich, M. Kianinia, C. Bradac, I. Aharonovich, V. Dyakonov, Room temperature coherent control of spin defects in hexagonal boron nitride. *Sci. Adv.* **7**, eabf3630 (2021).
17. S. Mañas-Valero, Y. C. Doedes, A. Bondarenko, M. Borst, S. Kurdi, T. Poirier, J. H. Edgar, V. Jacques, Y. M. Blanter, T. van der Sar, Isofrequency spin-wave imaging using color center magnetometry for magnon spintronics. *Nat. Commun.* **17**, 379 (2026).
18. S. Das, A. L. Melendez, I. H. Kao, J. A. García-Monge, D. Russell, J. Li, K. Watanabe, T. Taniguchi, J. H. Edgar, J. Katoch, F. Yang, P. C. Hammel, S. Singh, Quantum sensing of spin dynamics using boron-vacancy centers in hexagonal boron nitride. *Phys. Rev. Lett.* **133**, 166704 (2024).
19. W. Liu, V. Ivády, Z.-P. Li, Y.-Z. Yang, S. Yu, Y. Meng, Z.-A. Wang, N.-J. Guo, F.-F. Yan, Q. Li, J.-F. Wang, J.-S. Xu, X. Liu, Z.-Q. Zhou, Y. Dong, X.-D. Chen, F.-W. Sun, Y.-T. Wang, J.-S. Tang, A. Gali, C.-F. Li, G.-C. Guo, Coherent dynamics of multi-spin V_B^- center in hexagonal boron nitride. *Nat. Commun.* **13**, 5713 (2022).
20. P. Yu, H. Sun, M. Wang, T. Zhang, X. Ye, J. Zhou, H. Liu, C.-J. Wang, F. Shi, Y. Wang, J. Du, Excited-state spectroscopy of spin defects in hexagonal boron nitride. *Nano Lett.* **22**, 3545–3549 (2022).
21. S. Ru, L. An, H. Liang, Z. Jiang, Z. Li, X. Lyu, F. Zhou, H. Cai, Y. Yang, R. He, R. Cernansky, E. H. T. Teo, M. Mukherjee, A. A. Bettiol, J. Zúñiga-Perez, F. Jelezko, W. Gao, Room-temperature electrical readout of spin defects in van der Waals materials. *Phys. Rev. Lett.* **135**, 220802 (2025).
22. R. Rizzato, M. Schalk, S. Mohr, J. C. Hermann, J. P. Leibold, F. Bruckmaier, G. Salvitti, C. Qian, P. Ji, G. V. Astakhov, U. Kentsch, M. Helm, A. V. Stier, J. J. Finley, D. B. Bucher, Extending the coherence of spin defects in hBN enables advanced qubit control and quantum sensing. *Nat. Commun.* **14**, 5089 (2023).
23. M. Huang, J. Zhou, D. Chen, H. Lu, N. J. McLaughlin, S. Li, M. Alghamdi, D. Djugba, J. Shi, H. Wang, C. R. Du, Wide field imaging of van der Waals ferromagnet Fe_3GeTe_2 by spin defects in hexagonal boron nitride. *Nat. Commun.* **13**, 5369 (2022).
24. A. L. Melendez, R. Gong, G. He, Y. Wang, Y.-C. Wu, T. Poirier, S. Randolph, S. Ghosh, L. Liang, S. Jesse, A.-P. Li, J. T. Damron, B. J. Lawrie, J. H. Edgar, I. V. Vlassiouk, C. Zu, H. Zhao, Probing boron vacancy defects in hBN via single spin relaxometry. *Nat. Commun.* **17**, 3718 (2026).
25. T.-X. Zheng, M. I. Bakti Utama, X. Gao, M. Kar, X. Yu, S. Kang, H. Cai, T. Ruan, D. Ovetsky, U. Zvi, G. Lao, Y.-X. Wang, O. Raz, S. Chitransh, G. T. Smith, L. R. Weiss, M. H. Czyz, S. Yang, A. J. Fairhall, K. Watanabe, T. Taniguchi, D. D. Awschalom, A. P. Alivisatos, R. H. Goldsmith, G. C. Schatz, M. C. Hersam, P. C. Maurer, A surface-scaffolded molecular qubit. arXiv:2601.19976 [quant-ph] (2026).
26. X. Zhou, Y.-T. Kong, C. Kit Cheung, G. Bian, R. Moukaouine, K. C. Wong, Y. Sun, C.-I. Ho, V. Bushmakin, N. Gross, C.-C. Yen, T. Priessnitz, M. Lenger, S. Jayaram, T. Taniguchi, K. Watanabe, A. Pershin, R. Peng, Á. Gali, J. Smet, J. Wrachtrup, Optically addressable molecular spins at 2D surfaces. arXiv:2601.19988 [quant-ph] (2026).
27. N. Mathur, A. Mukherjee, X. Gao, J. Luo, B. A. McCullian, T. Li, A. N. Vamivakas, G. D. Fuchs, Excited-state spin-resonance spectroscopy of V_B^- defect centers in hexagonal boron nitride. *Nat. Commun.* **13**, 3233 (2022).
28. W. Liu, Z.-P. Li, Y.-Z. Yang, S. Yu, Y. Meng, Z.-A. Wang, Z.-C. Li, N.-J. Guo, F.-F. Yan, Q. Li, J.-F. Wang, J.-S. Xu, Y.-T. Wang, J.-S. Tang, C.-F. Li, G.-C. Guo, Temperature-dependent energy-level shifts of spin defects in hexagonal boron nitride. *ACS Photonics* **8**, 1889–1895 (2021).
29. R. O. Serha, C. Dubs, A. V. Chumak, Magnetic materials for quantum magnonics. *APL Mater.* **14**, 030901 (2026).
30. D. Lachance-Quirion, S. P. Wolski, Y. Tabuchi, S. Kono, K. Usami, Y. Nakamura, Entanglement-based single-shot detection of a single magnon with a superconducting qubit. *Science* **367**, 425–428 (2020).
31. Y. Tabuchi, S. Ishino, A. Noguchi, T. Ishikawa, R. Yamazaki, K. Usami, Y. Nakamura, Coherent coupling between a ferromagnetic magnon and a superconducting qubit. *Science* **349**, 405–408 (2015).
32. L. Ostermann, H. Ritsch, C. Genes, Protected state enhanced quantum metrology with interacting two-level ensembles. *Phys. Rev. Lett.* **111**, 123601 (2013).
33. S. Baber, R. N. E. Malein, P. Khatri, P. S. Keatley, S. Guo, F. Withers, A. J. Ramsay, I. J. Luxmoore, Excited state spectroscopy of boron vacancy defects in hexagonal boron nitride using time-resolved optically detected magnetic resonance. *Nano Lett.* **22**, 461–467 (2022).
34. A. Ariyaratne, D. Bluvstein, B. A. Myers, A. C. B. Jayich, Nanoscale electrical conductivity imaging using a nitrogen-vacancy center in diamond. *Nat. Commun.* **9**, 2406 (2018).
35. C. Du, T. van der Sar, T. X. Zhou, P. Upadhyaya, F. Casola, H. Zhang, M. C. Onbasli, C. A. Ross, R. L. Walsworth, Y. Tserkovnyak, A. Yacoby, Control and local measurement of the spin chemical potential in a magnetic insulator. *Science* **357**, 195–198 (2017).
36. Z. Hu, Z. He, Q. Wang, C.-T. Chou, J. T. Hou, L. Liu, Nonlinear magnetic sensing with hybrid nitrogen-vacancy/magnon systems. *Nano Lett.* **24**, 15731–15737 (2024).
37. B. A. McCullian, A. M. Thabt, B. A. Gray, A. L. Melendez, M. S. Wolf, V. L. Safonov, D. V. Pelekhov, V. P. Bhallamudi, M. R. Page, P. C. Hammel, Broadband multi-magnon relaxometry using a quantum spin sensor for high frequency ferromagnetic dynamics sensing. *Nat. Commun.* **11**, 5229 (2020).
38. H.-X. Zang, W. Jiang, N.-J. Guo, Y. Liu, M.-Q. Ma, Z.-W. Liu, L.-K. Shan, Y. Dong, S.-C. Zhang, J.-S. Tang, X.-D. Chen, G.-C. Guo, F.-W. Sun, Detecting and imaging of magnons at nanoscale with van der Waals quantum sensor. *Adv. Funct. Mater.* **35**, 2412166 (2025).
39. V. Williams, J. M. Nair, Y. Tserkovnyak, B. Flebus, Generating single-and many-body quantum magnonic states. arXiv:2507.05971 [cond-mat.mes-hall] (2025).
40. A. V. Chumak, V. I. Vasyuchka, A. A. Serga, B. Hillebrands, Magnon spintronics. *Nat. Phys.* **11**, 453–461 (2015).
41. S. O. Demokritov, V. E. Demidov, O. Dzyapko, G. A. Melkov, A. A. Serga, B. Hillebrands, A. N. Slavin, Bose–Einstein condensation of quasi-equilibrium magnons at room temperature under pumping. *Nature* **443**, 430–433 (2006).
42. T. Liu, J. Kally, T. Pillsbury, C. Liu, H. Chang, J. Ding, Y. Cheng, M. Hilse, R. Engel-Herbert, A. Richardella, N. Samarth, M. Wu, Changes of magnetism in a magnetic insulator due to proximity to a topological insulator. *Phys. Rev. Lett.* **125**, 017204 (2020).
43. S. Guo, D. Russell, J. Lanier, H. Da, P. C. Hammel, F. Yang, Strong on-chip microwave photon–magnon coupling using ultralow-damping epitaxial $Y_3Fe_5O_{12}$ films at 2 K. *Nano Lett.* **23**, 5055–5060 (2023).
44. C. Bradac, M. T. Johnsson, M. van Breugel, B. Q. Baragiola, R. Martin, M. L. Juan, G. K. Brennen, T. Volz, Room-temperature spontaneous superradiance from single diamond nanocrystals. *Nat. Commun.* **8**, 1205 (2017).
45. A. Angerer, K. Streltsov, T. Astner, S. Putz, H. Sumiya, S. Onoda, J. Isoya, W. J. Munro, K. Nemoto, J. Schmiedmayer, J. Majer, Superradiant emission from colour centres in diamond. *Nat. Phys.* **14**, 1168–1172 (2018).
46. J. Zou, S. K. Kim, Y. Tserkovnyak, Tuning entanglement by squeezing magnons in anisotropic magnets. *Phys. Rev. B* **101**, 014416 (2020).

47. L. J. Cornelissen, J. Liu, R. A. Duine, J. B. Youssef, B. J. van Wees, Long-distance transport of magnon spin information in a magnetic insulator at room temperature. *Nat. Phys.* **11**, 1022–1026 (2015).
48. K. Koshino, S. Kono, Y. Nakamura, Protection of a qubit via subradiance: A Josephson quantum filter. *Phys. Rev. Appl.* **13**, 014051 (2020).
49. L. Thiel, Z. Wang, M. A. Tschudin, D. Rohner, I. Gutiérrez-Lezama, N. Ubrig, M. Gibertini, E. Giannini, A. F. Morpurgo, P. Maletinsky, Probing magnetism in 2D materials at the nanoscale with single-spin microscopy. *Science* **364**, 973–976 (2019).
50. M. L. Palm, C. Ding, W. S. Huxter, T. Taniguchi, K. Watanabe, C. L. Degen, Observation of current whirlpools in graphene at room temperature. *Science* **384**, 465–469 (2024).
51. S. Liu, R. He, L. Xue, J. Li, B. Liu, J. H. Edgar, Single crystal growth of millimeter-sized monoisotopic hexagonal boron nitride. *Chem. Mater.* **30**, 6222–6225 (2018).
52. E. Janzen, H. Schutte, J. Plo, A. Rousseau, T. Michel, W. Desrat, P. Valvin, V. Jacques, G. Cassabois, B. Gil, J. H. Edgar, Boron and nitrogen isotope effects on hexagonal boron nitride properties. *Adv. Mater.* **36**, e2306033 (2024).
53. D. G. Purdie, N. M. Pugno, T. Taniguchi, K. Watanabe, A. C. Ferrari, A. Lombardo, Cleaning interfaces in layered materials heterostructures. *Nat. Commun.* **9**, 5387 (2018).
54. L. Rondin, J. P. Tetienne, T. Hingant, J. F. Roch, P. Maletinsky, V. Jacques, Magnetometry with nitrogen-vacancy defects in diamond. *Rep. Prog. Phys.* **77**, 056503 (2014).
55. G. Q. Yan, S. Li, H. Lu, M. Huang, Y. Xiao, L. Wernert, J. A. Brock, E. E. Fullerton, H. Chen, H. Wang, C. R. Du, Quantum sensing and imaging of spin–orbit-torque-driven spin dynamics in the non-collinear antiferromagnet Mn_3Sn. *Adv. Mater.* **34**, 2200327 (2022).
56. A. Rustagi, I. Bertelli, T. Van Der Sar, P. Upadhyaya, Sensing chiral magnetic noise via quantum impurity relaxometry. *Phys. Rev. B* **102**, 220403 (2020).
57. B. A. Kalinikos, A. N. Slavin, Theory of dipole-exchange spin wave spectrum for ferromagnetic films with mixed exchange boundary conditions. *J. Phys. C Solid State Phys.* **19**, 7013–7033 (1986).
58. M. O. Scully, M. S. Zubairy, *Quantum Optics* (Cambridge University Press, 2012).
59. R. H. Lehmberg, Radiation from an N-atom system. I. General formalism. *Phys. Rev. A* **2**, 883–888 (1970).
60. A. Asenjo-Garcia, M. Moreno-Cardoner, A. Albrecht, H. J. Kimble, D. E. Chang, Exponential improvement in photon storage fidelities using subradiance and "selective radiance" in atomic arrays. *Phys. Rev. X* **7**, 031024 (2017).
61. S. J. Masson, I. Ferrier-Barbut, L. A. Orozco, A. Browaeys, A. Asenjo-Garcia, Many-body signatures of collective decay in atomic chains. *Phys. Rev. Lett.* **125**, 263601 (2020).
62. M. Gross, S. Haroche, Superradiance: An essay on the theory of collective spontaneous emission. *Phys. Rep.* **93**, 301–396 (1982).
63. R. H. Dicke, Coherence in spontaneous radiation processes. *Phys. Rev.* **93**, 99–110 (1954).
64. G. Ferioli, I. Ferrier-Barbut, A. Browaeys, Emergence of second-order coherence in the superradiant emission from a free-space atomic ensemble. *Phys. Rev. Lett.* **134**, 153602 (2025).
65. S. Fuchs, A. Vukics, S. Y. Buhmann, Superradiance from nonideal initial states: A quantum trajectory approach. *Phys. Rev. A* **103**, 043712 (2021).
66. W. Lee, V. S. Liu, Z. Zhang, S. Kim, R. Gong, X. Du, K. Pham, T. Poirier, Z. Hao, J. H. Edgar, P. Kim, C. Zu, E. J. Davis, N. Y. Yao, Intrinsic high-fidelity spin polarization of charged vacancies in hexagonal boron nitride. *Phys. Rev. Lett.* **134**, 096202 (2025).
67. T. Clua-Provost, Z. Mu, A. Durand, C. Schrader, J. Happacher, J. Bocquel, P. Maletinsky, J. Fraunié, X. Marie, C. Robert, G. Seine, E. Janzen, J. H. Edgar, B. Gil, G. Cassabois, V. Jacques, Spin-dependent photodynamics of boron-vacancy centers in hexagonal boron nitride. *Phys. Rev. B* **110**, 014104 (2024).

Acknowledgments: We are grateful to Y. Tserkovnyak for insightful discussions. **Funding:** The quantum sensing measurements are supported by the Office of Naval Research (ONR) under grant no. N00014-23-1-2146. Development of millikelvin quantum microscopy is based upon work supported by the Air Force Office of Scientific Research under award number FA9550-25-1-0082. Device fabrications are supported by the US National Science Foundation under award nos. DMR-2437294, ECCS-2445826, and ECCS-2525800. B.F. and J.M.P.N. acknowledge support from DOE under award no. DE-SC0024090. J.H.E. and T.P. thank the National Science Foundation for supporting the $h^{10}B^{15}N$ crystal growth under award no. 2413808. Neutron irradiation of the $h^{10}B^{15}N$ is supported by the US Department of Energy, Office of Nuclear Energy, under DOE Idaho Operations Office Contract DE-AC07-05ID14517 as part of the Nuclear Science User Facilities award no. 24-4911. S.R. and Z.J. thank the NASA Solar System Exploration Research Virtual Institute (SSERVI), under cooperative agreement number NNH22ZDA020C (CLEVER, grant number: 80NSSC23M022), for the synthesis of ^{10}B-enriched monoisotopic hBN crystals. **Author contributions:** L.-J.Z. performed the quantum sensing measurements and analyzed the data with S.L. J.M.P.N. and B.F. developed the theory on magnon-mediated correlated relaxation dynamics of spin ensembles. Y.Z., Z.X., and J.Z. contributed to the device fabrication processes. T.P. and J.H.E. provided the isotopically purified $h^{10}B^{15}N$ crystals with different neutron irradiation doses. S.R. and Z.J. provided the monoisotopic $h^{10}BN$ crystals. H.W. contributed to discussion and data interpretation. C.R.D. supervised this project. **Competing interests:** The authors declare that they have no competing interests. **Data, code, and materials availability:** All data and code needed to evaluate and reproduce the results in the paper are present in the paper and/or the Supplementary Materials. The isotopically purified $h^{10}B^{15}N$ crystals used in this study are available from Kansas State University pending a material transfer agreement. Requests can be made to edgarjh@k-state.edu.

Submitted 3 June 2026
Accepted 27 October 2026
Published 27 November 2026
10.1126/sciadv.aej3973